

Numerical investigation of cavitation-regimes in a converging-diverging nozzle

¹Polina Gorkh, ¹Steffen J. Schmidt, and ¹Nikolaus A. Adams

¹*Institute of Aerodynamics and Fluid Mechanics, Department of Mechanical Engineering, Technical University of Munich*

Abstract

In the present study the authors analyze cavitation dynamics, instabilities and detachment mechanisms in an axisymmetric converging-diverging nozzle. Numerical simulation is used to investigate a recent experiment. Following the experimental setup, three operating points are simulated to identify two different cloud detachment mechanisms: re-entrant jet and condensation shock. A homogeneous mixture model is applied to model cavitating two-phase flows. Pure liquid and liquid-vapor mixtures are both treated as fully compressible substances to enable the computation of propagating pressure waves into the liquid bulk. Because the study focuses on inertia-dominated mechanisms, the flow is modeled as inviscid.

Our numerical simulation predicts a slightly different cavitation behavior than the one published for the reference experiment. We observe a high-frequency shedding that generates vapor pockets inside the channel. These vapor pockets partially collapse but frequently they integrate into a large coherent structure. Once a coherent vapor cloud reaches a sufficient length, it detaches and is advected downstream. As a result, the total vapor volume fraction shows a low frequency oscillation which is about one order slower than the shedding frequency. Two detachment mechanisms are present during one cycle: the re-entrant jet for shorter cavities and the condensation shock for longer cavities. The maximum cavity length is not constant but features significant cycle-to-cycle variation. Even a slight difference in the cavitation number leads to a difference in the detachment mechanisms: the lower cavitation number leads to a bubbly shock as the dominant detachment mechanism, while for a higher cavitation number shock-driven detachment occurs only once per cycle.

Keywords: cavitation, multi-phase flow, homogeneous mixture, nozzle flow

Introduction

In a broad range of fluidic applications, such as hydraulic machinery or diesel injection systems, understanding and assessment of transient cavity dynamics play a key role. In liquids, cavitation occurs when the pressure drops beneath a certain level. It can decrease machinery performance, cause pressure oscillations and, moreover, may lead to material erosion during the re-condensation process. Thus, prediction and investigation of various cavitation regimes are important.

Two main mechanisms cause the periodic cloud-detachment process: the classical re-entrant jet as described i.e. in [1], and condensation shock waves, propagating through a two-phase medium, as recently investigated in [2]. The latter can appear because the speed of sound within a two-phase mixture is significantly lower than within any of the pure states. Recent experimental observations of condensation shocks resulting in periodic shedding have been published for the case of a sharp-edged wedge [3]. In [4], the authors performed a simulation, proving that, for some boundary conditions, cloud detachment is dominated by the periodic occurrence of a bubbly shock wave.

In another recent study [5], the authors conducted flow experiments in a converging-diverging axisymmetric nozzle. Their findings are used in this work as the experimental reference. In [5], the authors applied high-speed imaging techniques to investigate three test cases with decreasing cavitation numbers. Depending on the cavitation number, they observe three different processes: periodic shedding driven by the re-entrant jet, transitional aperiodic behavior, and periodic shedding driven by the condensation shock wave.

The present study provides a numerical simulation of the convergent-divergent nozzle flow, accompanied by a further analysis of transient cavity dynamics and cavitation patterns. The numerical simulation reproduces the conditions of the reference experiment at all three operating points in order to assess different shedding mechanisms. Quantitative measurements of vapor volume frequencies, shedding frequencies, and the cavity length are compared to experimental data. In comparison with the wedge experiment, where the flow can be captured from the top or from the side, high-speed imaging of the axisymmetric flow lacks this opportunity. In contrast, simulation results allow to analyze complex 3-D flow features inside the axisymmetric nozzle.

Numerical Method

A density-based Finite Volume Method (FVM) is used in the simulations. A homogeneous mixture model [6] is applied to model the mixture region between liquid water and water vapor. All phases are modeled as being compressible to enable propagation of the pressure waves into the liquid bulk. Thermodynamic equilibrium is assumed; water is modeled as a

barotropic fluid. Phase change from pure liquid to saturated mixture is assumed to follow an equilibrium isentrope. The study is focused on inertia-dominated mechanisms, so the flow is modeled as inviscid. Solved and non-condensable gas is neglected.

The governing equations are the compressible Euler equations in conservative form. These are discretized on a 4-cell stencil for computational efficiency on structured body-fitting grids. A 4-stage 2-nd order Runge-Kutta method is used. Pressure dependency of density is described by modified Tait equation for pure liquid state [7] and is obtained by integrating the equilibrium speed of sound $c^2 = \frac{\partial p}{\partial \rho}_s$. The vapor volume fraction α is computed by $\alpha = (\rho - \rho_{l,sat}(T)) / (\rho - \rho_{v,sat}(T))$, where $\rho_{l,sat}$ and $\rho_{v,sat}$ are saturation densities of liquid and vapor phases, respectively.

Numerical Setup

The baseline experimental facility is described in [5] in detail. A schematic of the test section is shown in Figure 1 - all dimensions are given in *mm*. Flow direction is from left to right. The convergence and divergence angles are 36° and 16° , respectively. The diameter of the pipe section is 50 mm . The throttle diameter is $16,67\text{ mm}$ and the diameter of the exit is 50 mm . This leads to an area ratio of 1:9. The authors who performed the experiments kindly provided mass flux data at the inlet, from which uniform inflow velocities were computed and used as boundary conditions for the simulations. The inflow velocities, as well as the outlet pressure and the temperature in the domain (all measured in the experiments and used for our simulation) are summarized in Table 1 for three cases: re-entrant jet cavities detachment mechanism (Case 1), transition (Case 2), and condensation shock-induced cavity detachment mechanism (Case 3) [5].

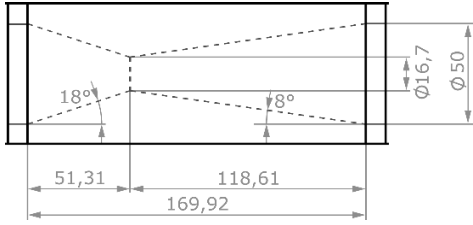


Figure 1: Test section geometry.

	$u_{in}, m/s$	P_{out}, Pa	T, K
(1) re-entrant jet	1,479	80580	287,66
(2) transition	1,578	80050	288,97
(3) condensation shock	1,525	25701	292,28

Table 1: Boundary and initial conditions.

In the experiments, pipe sections are added upstream and downstream of the test section. For the simulation, a pipe section ($l = 0.50\text{ m}$) is added in front of the test section and a second one ($l = 0.83\text{ m}$ for Cases 1 and 2 and $l = 1.08\text{ m}$ for Case 3) is added to the end of the test section (see Figure 2(a)). The computational domain for the latter case is longer, because the predicted cavitation length is larger than for the two other cases. For the same reason, the grid in the diverging region for the latter case is finer – see Figures 2(b) and 2(c) for a comparison of the meshes. Grid cells decrease in height toward the walls as water vapor is experimentally predicted to appear mainly close to the walls. The resulting cross-section topology along the whole domain can be seen in Figure 2(d).

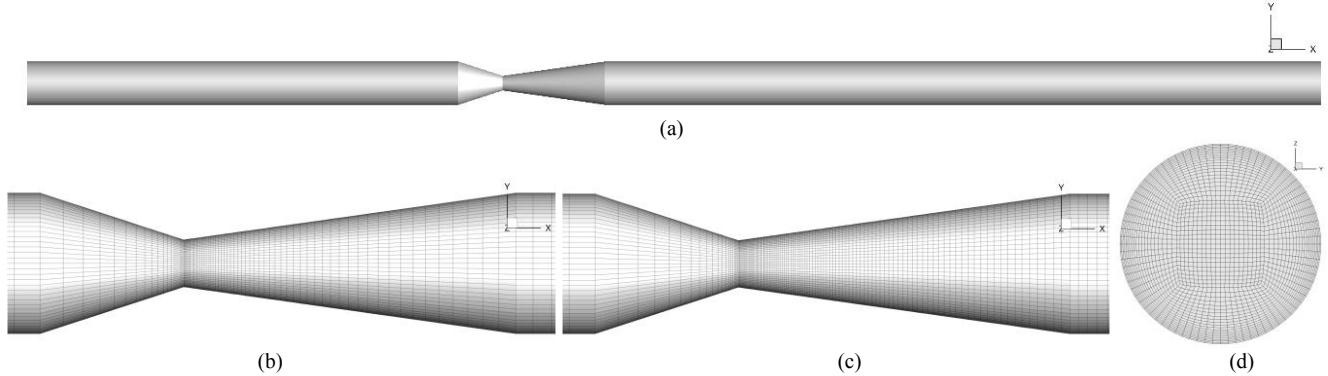


Figure 2: (a): Overview of the entire computational domain for re-entrant jet and transition cases; (b), (c): numerical grid in the vicinity of the throat, (b): for the re-entrant jet and transition cases, (c): for the condensation shock case; (d): grid cross-section.

To speed up the computations, grid sequencing was used: results from a coarser grid level are used as restart data for the finer grid level. In order to ensure suitable initial conditions, conservative interpolation techniques are applied. Mesh sizes for the final grid level are 280k cells for Case 1 and 2, and 400k cells for Case 3. Simulations on coarse grids were performed to establish statistically converged pressure and velocity distributions.

Results and Discussion

Several definitions of the cavitation number can be found in the literature. The definition $\sigma = (p - p_{sat}) / (\frac{1}{2}\rho u^2)$ is

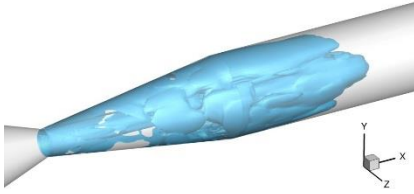


Figure 3: Instantaneous vapor volume fraction for case 3: vapor propagates into the pipe.

case	$P_{in,exp}, Pa$	$P_{in,sim}, Pa$
1	100277.6	130259
2	120469.9	145924
3	110383.6	124379

Table 2: Pressure at the inlet, measured in the reference experiment and in the simulation.

f_{exp}, Hz	L_{exp}, mm	f_{sim}, Hz	L_{sim}, mm
298.6586	15.9	251.1	13 - 37
101.1151	23.1	198.0	16 - 45

Table 3: Comparison of shedding frequencies and maximum cavity length in reference experiments and present simulations.

commonly used [8]. Here, p and u are pressure and velocity at the reference point, respectively (usually upstream of the cavitating region). However, for venturi flows, $p = p_{out}$ is typically chosen [5]. In this case, density and (uniform) velocity at the inlet, as well as the static pressure at the outlet, affect the cavitation number. The static pressure at the inlet is not taken into account into the cavitation number, although it is one of the most important quantities.

Our simulations predict higher pressures at the inlet than in the reference experiments (see Table 2). This raises the pressure difference between inflow and outflow and increases the driving force, which results in longer cavities and lower shedding frequencies. For Case 3, vapor structures are significantly elongated as compared to the reference experiment. The coherent vapor structures even exceed the divergence region and are propagating into the pipe region (see Figure 3). Up to now, we do not have a profound explanation for this behavior and thus, we excluded Case 3 from this report. In the following, our focus is put on Cases 1 and 2.

Figures 4(a) and 4(d) show the temporal development of the vapor volume fraction for Cases 1 and 2, respectively. An FFT of this data (Figures 4(b) and 4(e)) yields frequencies of $27.9 Hz$ and $22.0 Hz$, which are significantly lower than in the reference experiments. As expected, the frequency is lower for the lower cavitation number (Case 2).

For cases 1 and 2, with an equal number of time steps, Figures 4(c) and 4(f) show an x-t-diagram of axially integrated vapor volume fraction α , computed at the divergent part of the nozzle. As the computational time steps are identical for Cases 1 and 2 ($28.3 ns$), the durations of the corresponding x-t-diagrams are comparable as well.

Figure 4(a) indicates a single frequency in the “vapor-volume versus time” graph ($f = 27.9 Hz$, peak frequency shown in Figure 4(b)), which is much lower than the experimental shedding frequency. However, in Figure 4(c) an x-t diagram of the shedding is plotted (in a vertical orientation) covering just about 1.3 periods. Multiple shedding processes are visible – although the integrated vapor volume fraction undergoes just one single oscillation! Figures 4(a) and 4(b), do not show the

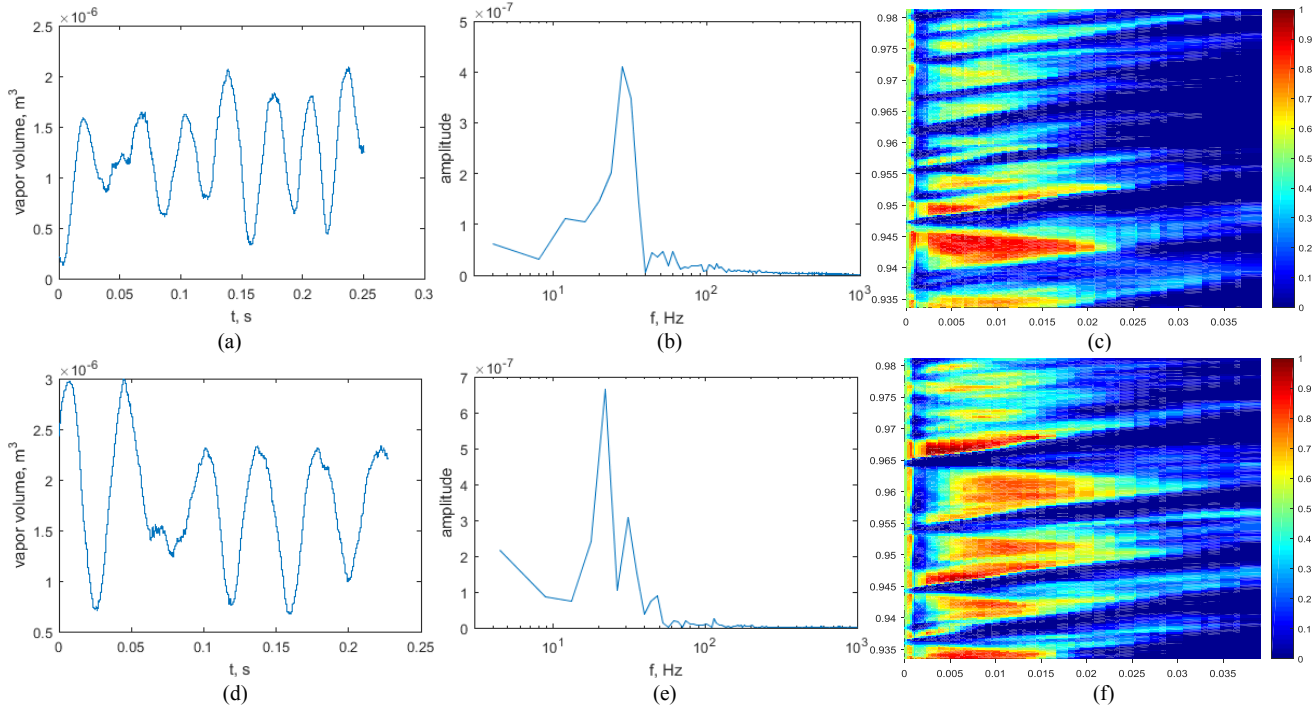


Figure 4: (a), (d): Vapor volume fraction development for Cases 1 and 2, respectively; (b), (e): FFT of vapor volume fraction for Cases 1 and 2, respectively; (c), (f): x-t-diagram of axially integrated vapor volume fraction for Cases 1 and 2, respectively.

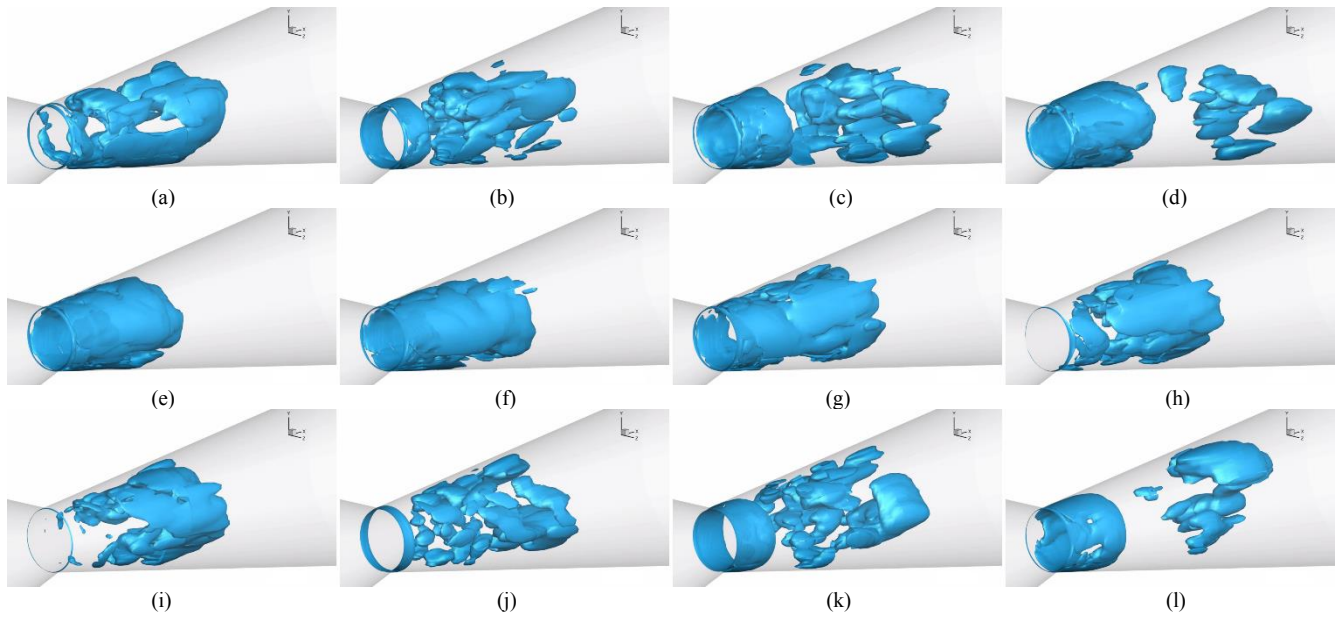


Figure 5: Development and shedding of two vapor clouds for Case 2 with different detachment mechanisms.

shedding frequency but an accumulated low frequency behavior. It entirely hides the shedding process which is visible on the x - t diagram of the cavity length (Figure 4 (c)). The process “hidden” in Figures 4(a) and 4(b) has a much higher frequency and agrees much better to the experimental observations of the shedding frequency.

Our interpretation is as follows: The high frequency shedding generates vapor pockets inside the channel. These pockets sometimes collapse, but mostly they integrate into larger vapor clouds. Once such a vapor cloud reaches a sufficient length, it detaches and is advected downstream. This causes the low frequent oscillation of the integrated vapor volume fraction. For both Cases, 1 and 2, two detachment mechanisms are present during the same cycle: re-entrant jet for shorter cavities (i.e. at $t = 965 \text{ ms}$ and $t = 975 \text{ ms}$ for Case 1, Figure 4(c)) and condensation shock for longer cavities (i.e. at $t = 943 \text{ ms}$ for Case 1, Figure 4(c)). However, the maximum cavity length is not constant but features a strong cycle-to-cycle variation.

In contrast to the reference experiment, both mechanisms, the re-entrant jet and the condensation shock, are simultaneously present in both simulations. Case 1 features just one instance of a condensation shock, while Case 2 shows 3-4 such instances. Using x - t -diagrams, one can count the approximate number of shedding processes and then compute the shedding frequencies. We obtain 251 Hz for Case 1 and 198 Hz for Case 2. These frequencies and cavity lengths are compared to the reference data in Table 3.

Figure 5 demonstrates the formation of cavitation patterns for Case 2 for a time span ranging from 954.5 ms to 968.5 ms . This time period includes two shedding processes (see Figure 4(f)): one shock-induced detachment (Figures 5(a)-5(i)), and afterwards one re-entrant jet detachment (Figures 5(i)-5(l)). Figure 5(a) at $t = 954.47 \text{ ms}$ shows a previous cavity that has just detached and a new one is starting to form. Its development is shown in Figures 5(b), 5(c), and 5(d), until it reaches a length of $L = 33 \text{ mm}$ at $t = 960,90 \text{ ms}$, see Figure 5(e). After that, a bubbly shock starts to propagate upstream through the vapor cloud (Figures 5(f), 5(g), 5(h)). Detachment of the cloud appears at 964.48 ms , reaching a maximum length $L_{max} \approx 45 \text{ mm}$, captured in Figure 5(i). Next, the new cavity starts to grow. This process is shown in Figures 5(j) and 5(k). A second shedding process, in this case induced by a re-entrant jet, happens at $t = 958.62 \text{ ms}$. It is shown in Figure 5(l).

Acknowledgments

This study is part of a project that has received funding from the European Union's Horizon 2020 research and innovation programme under grant agreement № 642536. The authors gratefully acknowledge the Gauss Centre for Supercomputing e.V. (www.gauss-centre.eu) for funding this project by providing computing time on the GCS Supercomputer SuperMUC at Leibniz Supercomputing Centre (www.lrz.de). The authors further greatly acknowledge Mr. Saad Jahangir and Mr. William Hogendoorn from Delft University of Technology for sharing experimental data and for fruitful discussions on the subject.

References

- [1] Franc, J.-P., Michel, J.-M. (2005). *Fundamentals of Cavitation*. Springer Science + Business Media.
- [2] Ganesh, H. (2015). *Bubbly shock propagation as a cause of sheet to cloud transition of partial cavitation and stationary cavitation bubbles forming on a delta wing vortex*. Ph.D. thesis, University of Michigan.

- [3] Ganesh, H., Mäkiharju, S., Ceccio, S. (2016). *Bubbly shock propagation as a mechanism for sheet-to-cloud transition of partial cavities*. Journal of Fluid Mechanics. 802.
- [4] Budich, B., Neuner, S., Schmidt, S., Adams, N. (2015). *Numerical investigation of shedding partial cavities over a sharp wedge*. Journal of Physics: Conference Series. 656.
- [5] Hogendoorn, W. (2017) *Experimental investigation of cavitation regimes in a converging-diverging nozzle*. Master's Thesis, Delft University of Technology.
- [6] Schmidt, S., Thalhamer, M., Schnerr, G. (2009). *Inertia controlled instability and small scale structures of sheet and cloud cavitation*. 7th International Symposium on Cavitation, CAV2009, Michigan, USA.
- [7] Sezal, I. (2009). *Compressible dynamics of cavitating 3-D multi-phase flows*. Ph.D Thesis, Technische Universität München.
- [8] Brennen, C. (2013). *Cavitation and bubble dynamics*. Cambridge University Press.
- *Corresponding Author, Polina Gorkh: polina.gorkh@tum.de